Multiple Competing Magnetic Interactions in $Na_4Ni_7(PO_4)_6$

*Qingbo Xia[1,†], Chun-Hai Wang[2,†], Siegbert A. Schmid[1], Maxim Avdeev[1,3], and Chris D. Ling[1,]**

[†] *Joint first-author with equal contributions*
[1] School of Chemistry, The University of Sydney, Sydney 2006, Australia
[2] State Key Laboratory of Solidification Processing, School of Materials Science and Engineering, Northwestern Polytechnical University, Xi'an, Shaanxi 710072, China
[3] Australian Centre for Neutron Science, Australian Nuclear Science and Technology Organisation, Kirrawee 2232, Australia

Abstract

The low-temperature magnetic behavior and ground state of the candidate sodium-ion battery cathode compound $Na_4Ni_7(PO_4)_6$, have been investigated by physical property measurements and neutron powder diffraction. On cooling, $Na_4Ni_7(PO_4)_6$ undergoes three successive long-range spin ordering transitions to Phase I (below T_N = 17 K), Phase II (below T_N' = 9.1 K) and Phase III (below T_N'' = 4.6 K) with ordering vectors [0, 1, 1/2], [0, 2/3, 1/2], and [~0.076, 2/3, 1/2], respectively. All three magnetic phases can be described in terms of ferromagnetic Ni^{2+} stripes with antiferromagnetic interactions between them. The moment amplitude of all stripes is the same in Phase I but varies in Phase II, while Phase III is an incommensurate variation on Phase II. Phases I and II both feature a crystallographically unique Ni site with no ordered magnetic moment due to geometric frustration, the resolution of which may be the driving force behind the final transition to Phase III. Even among transition metal phosphates, which typically show complex spin ordering due to competition between superexchange and super-superexchange (through PO_4 linkers), $Na_4Ni_7(PO_4)_6$ has one of the richest magnetic phase diagrams explored so far.

Introduction

Sodium-ion batteries (NaIBs) are of intense current interest as alternatives to lithium-ion batteries (LIBs) for large-scale applications where kinetics (power) and weight are not the primary considerations.[1-2] The obvious example is load-leveling of intermittent renewably sourced energy. The jury is still out on the ultimate competitiveness of NaIBs versus other energy storage solutions, with one major uncertainty being a lack of Na electrode materials.[3-5] Inspired by $LiFePO_4$, sodium redox-active transition metal phosphates have been intensively investigated as possible high-energy-density, cheap, safe and environmentally friendly cathode candidates.[6-7] $Na_4Ni_7(PO_4)_6$ crystallizes in a monoclinic structure (space group $C1m1$, #8), and assumes a framework with non-centrosymmetric Na^+ inside.[8] The framework structure is formed by interconnected $[Ni_7(PO_4)_6]^{4+}$ layers with tunnels in between where the Na ions reside. These structural features make $Na_4Ni_7(PO_4)_6$ of interest as a potential NaIB electrode candidate.

In addition, sodium transition metal phosphates show a remarkable variety of magnetic properties and structures.[9-12] In the case of Ni^{2+} ([Ar]$3d^8$), the spin coupling is particularly subtle, involving a wide variety of superexchange (SE) and super-superexchange (SSE) interactions via PO_4 linkers

that generally give ferromagnetic (FM) nearest neighbor coupling and antiferromagnetic (AFM) second- and/or third-nearest neighbor coupling. The result is often a complex AFM arrangement of FM stripes or layers.[13-15] In the work reported here, we found that $Na_4Ni_7(PO_4)_6$ is one of the most complex cases reported so far. It undergoes three distinct low-temperature magnetic ordering transitions, corresponding to three distinct competing magnetic ground states.

The magnetic ground states of transition metal phosphates (and related polyanionic network compounds such as sulphates and silicates) are of fundamental interest because they show such a rich variety of SE and SSE pathways. As more cases are solved experimentally, the rules governing the sign and strength of SSE magnetic exchange become clearer and their predictive power improves. However, when these frameworks also contain sodium and lithium in topologies conducive to ionic conduction, their magnetic structures are relevant to understanding their performance as solid-state battery electrode materials: accurate *ab initio* calculations of their structures and Li/Na conduction dynamics depends on knowledge of the experimental electronic and magnetic ground state.

Experimental Details

$Na_4Ni_7(PO_4)_6$ was synthesized by a conventional solid-state reaction method. A stoichiometric mixture of $Na(CH_3COO)\bullet 2H_2O$, $Ni(CH_3COO)_2\bullet 4H_2O$ and $NH_4H_2PO_4$ was thoroughly milled and mixed in a planetary ball-mill at 360 rpm for 1 h. The fine power mixture was then heated in an open crucible at 400°C for 10 h (to decompose all initial reactants) and 900°C for 10 h [to crystallize $Na_4Ni_7(PO_4)_6$] in a muffle furnace with an intermediate re-grinding. The final product was ground again after cooling.

Temperature-dependent direct-current (DC) magnetic susceptibility data were collected in both zero field-cooled (ZFC) mode and field-cooled (FC) mode using a Quantum Design Physical Properties Measurement System (PPMS) with a Vibrating Sample Magnetometer (VSM) probe, under a 1000 Oe magnetic field between 300 K and 2 K. Low-temperature heat capacity (HC) measurements of $Na_4Ni_7(PO_4)_6$ were also carried out in the PPMS (under zero field) between 25 K and 2 K.

Neutron powder diffraction (NPD) measurements were carried out using the high-resolution diffractometer ECHIDNA[16] at the OPAL facility, Australian Nuclear Science and Technology Organisation (ANSTO), using neutrons of wavelength 2.4395 Å. The powder sample was sealed in a vanadium can and low-temperature data were collected between 2 K and 30 K. The magnetic structures were analyzed by Rietveld refinement using the TOPAS Academic (TA) software.[17-18] For the magnetic structure refinements, the nuclear structure model refined against 30 K NPD data was selected as the parent structure (undistorted) and symmetry representation analysis was applied using ISODISTORT[19] according to the observed magnetic supercell reflections.

Results and Discussion

Physical Property Measurements

Three turning points were observed in the temperature-dependent magnetic susceptibility curve of $Na_4Ni_7(PO_4)_6$, as shown in Fig. 1. A sharp downturn at T_N = 17 K clearly suggests antiferromagnetic (AFM) ordering below this temperature. Further downturns at $T_{N'}$ = 9.1 K and $T_{N''}$ = 4.6 K reveal successive magnetic phase transitions. There is no divergence between ZFC and FC data in any temperature regime (Fig. S1 in supplementary information), suggesting that all three AFM phases are long-range ordered. The inverse ZFC magnetic susceptibility curve is well-fitted in the high-temperature paramagnetic regime (100-300 K) by the Curie-Weiss law $\chi = C/(T - \Theta_{CW}) + \chi_0$, where χ_0 includes all temperature-independent contributions. The fitting yielded a Curie temperature Θ_{CW} = -10.1(8) K, χ_0 = 0.000379 emu/mol, and an effective moment $\mu_{eff} = 3.38(3)\mu_B$. The negative Curie temperature indicates predominantly AFM interactions in the system. The value of the experimentally obtained effective moment is higher than the expected spin-only moment for d^8 $S = 1$ Ni^{2+} ($\mu_{SO} = 2.83\ \mu_B$), but within the range of values (2.83-4.49 μ_B) typically observed for this ion due to incomplete quenching of orbital component.

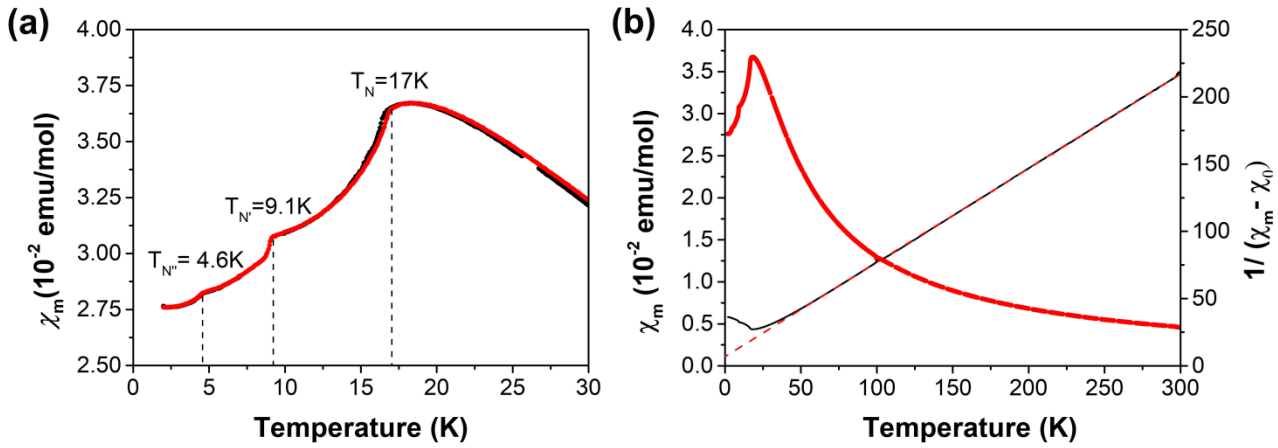

Fig. 1. *(a) Temperature-dependent ZFC and FC (red and black symbols, respectively) molar magnetic susceptibility* χ_m *of* $Na_4Ni_7(PO_4)_6$ *between 2 K and 30 K. (b) Inverse ZFC susceptibility* $1/(\chi_m - \chi_0)$ *(black line) as a function of temperature and its Curie-Weiss fit (red dash line)*

Heat capacity (HC) data in the low-temperature region covering the magnetic susceptibility features are presented in Fig. 2. Sharp exothermic peaks at 16.5 K and 8.6 K clearly correspond to T_N and $T_{N'}$ respectively. The shape of the peak at 16.5 K is typical for a lambda second-order transition, but the peak at 8.6 K (Dirac's delta shape) suggests a first-order transition, as do the magnetic susceptibility data (Fig. 1a). This suggests that on cooling, the Ni^{2+} moments first become magnetically long-range ordered at T_N, and then undergo a rearrangement to a distinctly different type of magnetic ordering at $T_{N'}$. In contrast, there is a conspicuous absence of any sharp HC peak corresponding to $T_{N''}$, suggesting a subtler and possibly continuous change in magnetic ordering at this temperature. The red line in Fig. 2 shows the integrated magnetic entropy $S(T)/R$ relative to the expected value of 7ln3 for seven Ni^{2+}($S = 1$) ions in the formula unit. We obtain 1.16 (~0.15 × 7ln3) at $T_{N'}$ = 8.6 K; 3.88 (~0.5 × 7ln3) at $T_{N''}$ = 16.5 K; and 7.04 (~0.9 × 7ln3) at 30 K, the est temperature at which we collected HC data. While these values are not definitive because the phonon contribution cannot be subtracted accurately (we do not have a non-magnetic analogue), they suggest short-range order above T_N, possibly due to competing magnetic exchange interactions.

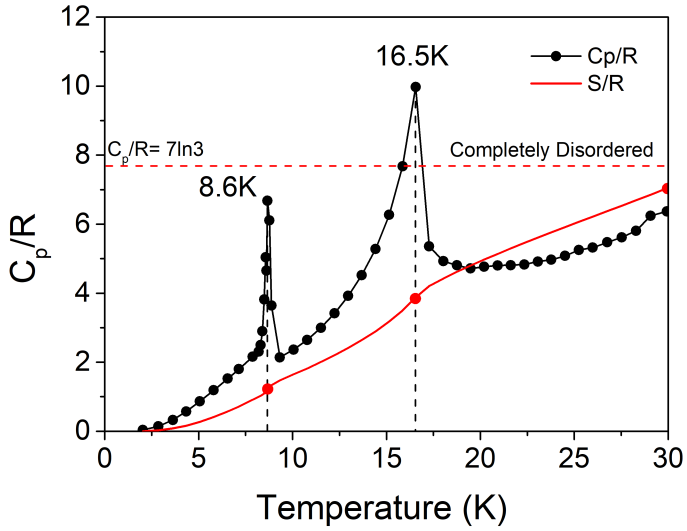

Fig. 2. *Heat capacity data for $Na_4Ni_7(PO_4)_6$ between 2 K and 30 K, showing exothermic peaks at 16.5 K and 8.6 K (cf. T_N = 17 K and $T_{N'}$ = 9.1 K in the magnetic susceptibility data in Fig. 1). The red line shows the integrated magnetic entropy approaching the expected value of 7ln(3) for the seven Ni^{2+} (S = 1) ions in the formula unit.*

Magnetic Structure Determination

Temperature-dependent neutron powder diffraction (NPD) patterns in the low-angle region (10-40°, 2θ) for $Na_4Ni_7(PO_4)_6$ are shown in Fig. 3. New Bragg reflections due to long-range magnetic ordering are clearly observed for $T \leq 14$ K. During cooling, an obvious magnetic peak appears at 2θ = 15.09(1)° in data collected between 14–9.5 K, grows gradually on cooling, then disappears suddenly again in data collected at 7.5 K and below, replaced by two new magnetic peaks at 2θ = 13.08(1)° and 17.54(1)°. This is consistent with a second-order long-range magnetic ordering at T_N = 17 K (16.5 K) followed by a first-order rearrangement to a different ordering at $T_{N'}$ = 9.1 K (8.6 K), in agreement with the magnetic susceptibility (HC) data presented above. As the temperature is lowered further, the two new magnetic peaks move and then "lock in" at 12.95(1)° and 17.74(1)° between 5.5–1.5 K. This continuous change is consistent with the change in magnetic susceptibility at $T_{N''}$ = 4.6 K but the absence of a corresponding HC peak.

Thus, we have identified three different long-range ordered magnetic phases of $Na_4Ni_7(PO_4)_6$ in terms of the relationship between the magnetic Bragg reflections and those of the nuclear structure: Phase I, from 9.1–17 K, with the magnetic ordering vector **k** = **b*** + (1/2) **c***; Phase II, from 4.6–9.1 K, with the magnetic ordering vector **k** = (2/3) **b*** + (1/2) **c***; and an incommensurate Phase III, below $T \leq 4.6$ K, with **k** = 0.076 **a*** + (2/3) **b*** + (1/2) **c***. Alternatively stated, the magnetic ordering vectors of Phase I, II, and III are [0, 1, 1/2], [0, 2/3, 1/2], and [~0.076, 2/3, 1/2], respectively. Note that the alternative vectors [0, 1/2, 0] and [0, 1/3, 1/2] were considered for Phase I and Phase II, respectively, but ruled out due to failing to index all magnetic peaks.

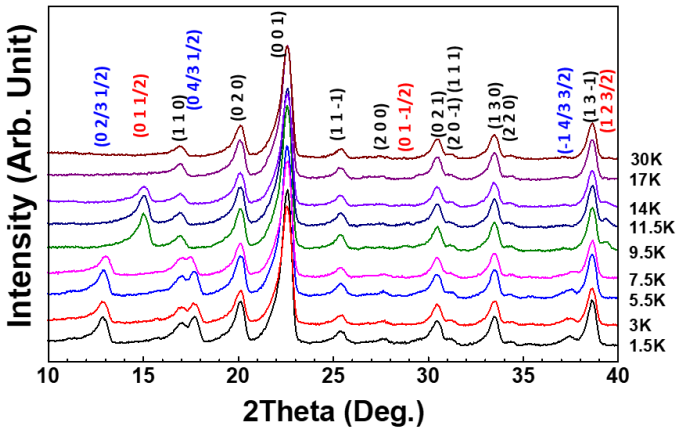

Fig. 3. *NPD patterns in the low-angle region for $Na_4Ni_7(PO_4)_6$ between 1.5 K and 30 K. Peaks are indexed according to the 30K nuclear structure.*

.

The nuclear structure of $Na_4Ni_7(PO_4)_6$ has a *C*-centred monoclinic unit cell and was Rietveld-refined against the 30 K NPD data, yielding the excellent profile fit shown in Fig. 4 with R_{wp} = 4.49%. Details of the nuclear structure model shown in Fig. 5 are given in the CIF file in the SI. It is essentially the same as the room-temperature structure reported by Moring and Kostiner.[8] The structure of $Na_4Ni_7(PO_4)_6$ can be described as layers of [NiO_6] octahedra and [PO_4] tetrahedra in the *a*-*b* plane, connected by [PO_4] tetrahedra to form the 3D framework. Na^+ ions occupy the channels between layers to provide electrostatic bonding and charge compensation.

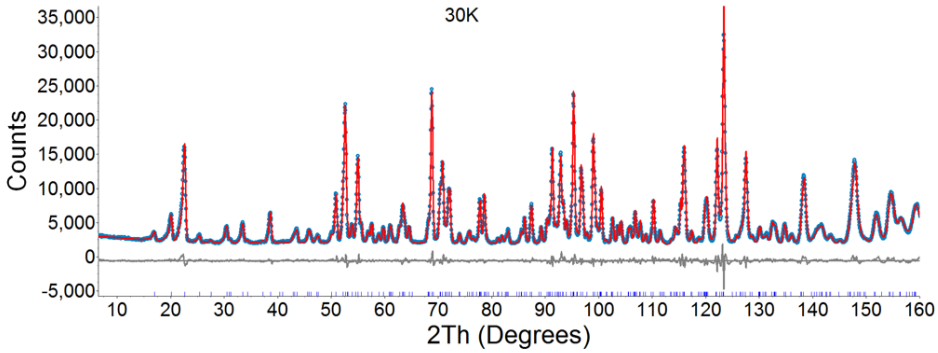

Fig. 4. *Rietveld refinement profiles of $Na_4Ni_7(PO_4)_6$ against 30 K NPD data. Dots, observed pattern; solid line, calculated pattern; grey line below, difference curve; vertical tick marks, peak positions.*

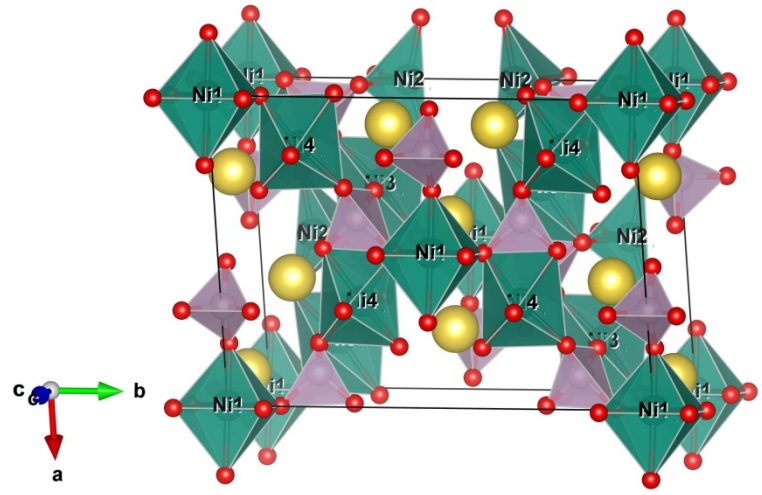

Fig. 5. *Nuclear structure of $Na_4Ni_7(PO_4)_6$ at 30 K from Rietveld-refinement against NPD data. NiO_6 octahedra are green, PO_4 tetrahedra are purple, and Na^+ ions are yellow.*

We used ISODISTORT[19] to analyse the spin ordering based on the group theory analysis (in terms of irreducible representations). The relationship between magnetic vector/reflections and the symmetry of the nuclear structure restricts the spin ordering (vector base) possibilities for the magnetic ions, which we used to simplify the analysis. The group theory analysis applied here covers the complete base (long-range spin ordering) of the distortion symmetry observed in the diffraction pattern. We considered possibilities where non-zero contributions to magnetic reflections could be extracted from the refinement.

Magnetic Phase I. The magnetic structure can be treated as a distortion of the nuclear structure, with the magnetic moment vectors as distortion parameters.[19] Thus, the magnetically ordered structures of $Na_4Ni_7(PO_4)_6$ were constructed from the 30 K nuclear structure model presented above. The distortion vector for Phase I is identified as **M** (0, 1, 1/2). There are two irreducible representations (IR) m$\mathbf{M}_1$ and m$\mathbf{M}_2$ from the group theory analysis when the magnetic moment of Ni^{2+} is considered.[19] The magnetic space groups (Shubnikov groups) of m$\mathbf{M}_1$ and m$\mathbf{M}_2$ are C_cm (8.35) and C_cc (9.40), respectively, and the magnetic unit cells of both models are double the nuclear ones, described by the transformation matrix [(1,0,2)(0,-1,0)(0,0,2)]. In the 30 K $Na_4Ni_7(PO_4)_6$ nuclear structure, there are four different Ni^{2+} Wyckoff sites: Ni1 (2*a*), Ni2 (4*b*), Ni3 (4*b*), and Ni4 (4*b*). The two different Wyckoff types give magnetic modes with different symmetries in each IR. In m$\mathbf{M}_1$, magnetic moment on the 2*a* site (of the nuclear structure model) gives the symmetry *A*' mode and that on the 4*b* site gives three different modes, A_1, A_2 and A_3. However, in m$\mathbf{M}_2$, the magnetic moment on the 2*a* site gives A_1" and A_2" modes and that on the 4*b* site also gives three different modes, A_1, A_2 and A_3. This gives ten independent magnetic moment modes in the m$\mathbf{M}_1$ model and eleven in the m$\mathbf{M}_2$ model. Details of these spin configurations are contained in the deposited CIFs and shown visually in Figure S2 of the SI.

The amplitudes of the different symmetry modes in the m$\mathbf{M}_1$ and m$\mathbf{M}_2$ models were refined against the 9.5 K NPD data. In the refinements, atomic coordinates were fixed to the 30 K nuclear structure model. The R_{wp} refinement factors are shown in Fig. 6. Both m$\mathbf{M}_1$ and m$\mathbf{M}_2$ models give good fits to the 9.5 K NPD data, with R_{wp} = 5.89% and 5.79% (*vs.* R_{wp} = 7.72% without magnetic modes)

when all magnetic modes are refined. The modes A_1 and A_2 in m$\mathbf{M}_1$ or the mode A_3 in m$\mathbf{M}_2$ were found to be the key magnetic distortion modes from these refinements: the structural model with only A_1 and A_2 modes (six magnetic parameters, A_1+A_2 in Fig. 6) in m$\mathbf{M}_1$ gives R_{wp} = 5.93% and the model with A_3 modes (three magnetic parameters) in m$\mathbf{M}_2$ gives R_{wp} = 5.80%. It should be noted that the A_1 and A_2 of m$\mathbf{M}_1$ model are orthogonal and correlated: they describe the moments in the *a*-*b* plane and give a similar fit to the experimental data, *i.e.*, the moments can be rotated together in the *a*-*b* plane. The amplitudes of A_1 and A_2 were constrained to be identical, so that we could refine both modes stably. This also has the effect of making the amplitude of magnetic moments directly comparable for both m$\mathbf{M}_1$ and m$\mathbf{M}_2$ models.

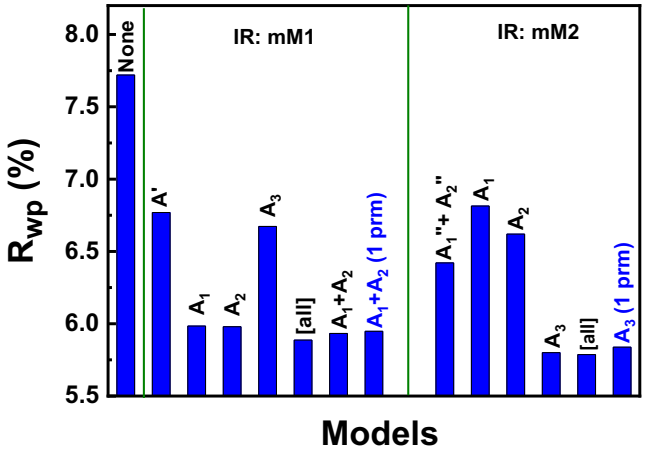

Fig. 6. *R_{wp} factors from the refinement of different magnetic structure models against 9.5 K NPD data. None (nuclear structure without magnetic moments); A', A_1", A_2", A_1, A_2, and A_3 (only the one type of moment modes considered in m$\mathbf{M}_1$ or m$\mathbf{M}_2$ model); [all] (all the modes considered in each IR); A_1 + A_2 (1 parameter, prm) (moment parameters reduced from six to one in m$\mathbf{M}_1$ with only A_1 and A_2 modes considered); A_3 (1 prm) (moment parameters reduced from three to one in m$\mathbf{M}_2$ with only A_3 modes considered). For further details see the discussion in the main text.*

A further refinement, with the same modes (A_1, A_2 or A_3) of Ni2, Ni3 and Ni4 (in terms of the 30 K nuclear structure) constrained to have the same amplitude, gave R_{wp} = 5.95% (m$\mathbf{M}_1$) and 5.84% (m$\mathbf{M}_2$). The R_{wp} of these models are labelled as A_1+A_2 (1 parameter, prm) for IR m$\mathbf{M}_1$ and A_3 (1 prm) for IR m$\mathbf{M}_2$ in Fig. 6. Compared to the model in which all modes were refined in m$\mathbf{M}_1$ or m$\mathbf{M}_2$, the m$\mathbf{M}_1$ A_1+A_2 (1 prm) and m$\mathbf{M}_2$ A_3 (1 prm) models give similar refinement results but the parameters used to describe the magnetic orders are greatly reduced. The constrained model is therefore preferred as it avoids over-parametrization relative to the limited number of observed magnetic reflections. The m$\mathbf{M}_1$ A_1+A_2 (1 prm) and m$\mathbf{M}_2$ A_3 (1 prm) models were therefore selected to interpret the magnetic Phase I of $Na_4Ni_7(PO_4)_6$ and will be referred to as the m$\mathbf{M}_1$ and m$\mathbf{M}_2$ models in the following discussions. The m$\mathbf{M}_2$ model is slightly better than the m$\mathbf{M}_1$ model in terms of R_{wp}, but not by enough to definitely rule out the m$\mathbf{M}_1$ model.

Rietveld refinement profiles for the m$\mathbf{M}_1$ and m$\mathbf{M}_2$ models against the 9.5 K NPD data are shown in

Fig. 7. Both the monoclinic models correctly predict the observed magnetic peaks. The refined cell parameters are listed in Table 1, which shows a good agreement for both models. Details of the refined structures are given in the magnetic CIF files in the SI. Refinements of magnetic Phase I at different temperatures were also performed, and the obtained cell parameters and Ni^{2+} moment amplitude at sites Ni2, Ni3, and Ni4 given in Table 1. There is no obvious change in the unit cell parameters but the magnetic moment amplitude increases from ~1.4 μ_B at 14 K to ~1.7 μ_B at 9.5 K.

The magnetic structures of m$\mathbf{M}_1$ and m$\mathbf{M}_2$ are shown in Fig. 8. The magnetic moments are represented as arrows. In each model, the magnetic moment of Ni1 (correlated to Ni1 in the 30 K nuclear structure) is 0 and the amplitudes of other Ni^{2+} (Ni2, Ni3, and Ni4) are the same, as listed in Table 1. As noted above, these Ni^{2+} magnetic moments have similar amplitudes in both models. The magnetic vectors in m$\mathbf{M}_1$ are aligned in the *a-c* plane while the vectors in m$\mathbf{M}_2$ are parallel to the *b* axis, *i.e.*, perpendicular to the *a-c* plane. However, the relative alignments of the moments in the two models are similar. The Ni^{2+} moments form FM stripes in the [101] direction (into the page as shown in Fig. 8), consistent with Goodenough-Kanamori superexchange (SE) rules for the continuous network of ~90° Ni–O–Ni pathways. These stripes are then arranged AFM in the [10-1] direction (vertical in Fig. 8), where they are coupled exclusively by super-superexchange (SSE) pathways through bridging PO_4 units; and also AFM in the [010] direction (horizontal in Fig. 8), where they are coupled by a more complex combination of SE and SSE pathways. The Ni1 site lies between AFM-coupled stripes, therefore its zero refined (ordered) magnetic moment can be ascribed to geometric magnetic frustration.

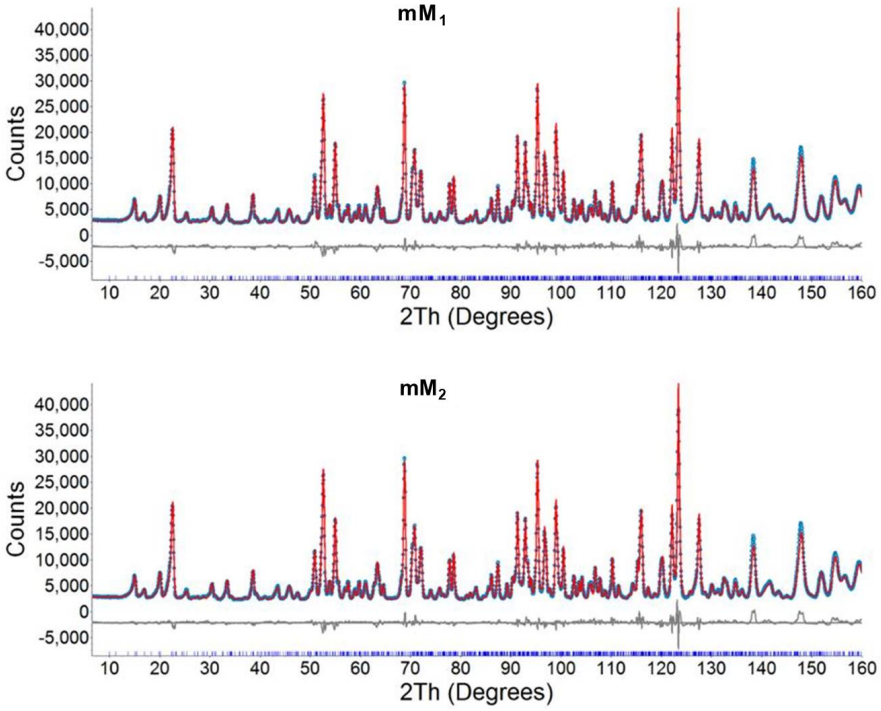

Fig. 7. *Rietveld refinement profiles of $Na_4Ni_7(PO_4)_6$ magnetic Phase I against 9.5 K NPD data using the m$\mathbf{M}_1$ and m$\mathbf{M}_2$ models. Dots, observed pattern ; solid line, calculated pattern; grey line below, difference curve; vertical tick marks, peak positions.*

Table 1. Refined cell parameters and Ni^{2+} magnetic moments (Ni2, Ni3, and Ni4) of $Na_4Ni_7(PO_4)_6$ magnetic Phase I from NPD data at 14 K, 11.5 K and 9.5 K.

IR	**mM$_1$**			**mM$_2$**		
T	14 K	11.5 K	9.5 K	14 K	11.5 K	9.5 K
a (Å)	14.4040(2)	14.4037(2)	14.4035(2)	14.4037(2)	14.4030(2)	14.4028(2)
b (Å)	13.9443(2)	13.9438(2)	13.9439(2)	13.9438(2)	13.9430(2)	13.9431(2)
c (Å)	12.8567(2)	12.8564(2)	12.8564(2)	12.8564(2)	12.8557(2)	12.8558(2)
β (°)	134.717(1)	134.717(1)	134.717(1)	134.718(1)	134.718(1)	134.718(1)
M (μ_B)	1.35(2)	1.63(2)	1.74(2)	1.40(2)	1.69(1)	1.79(2)

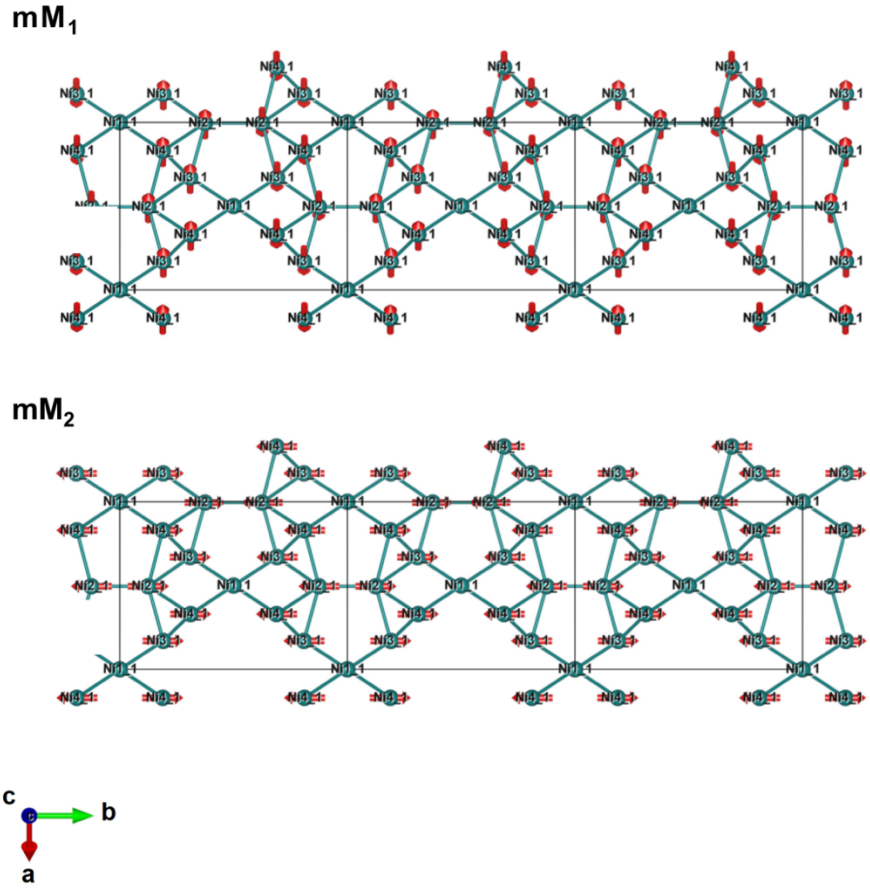

Fig. 8. *Single layers of the Rietveld-refined Phase I magnetic structures of $Na_4Ni_7(PO_4)_6$. Neighboring layers are AFM with respect to those shown. Only Ni sites are shown, with the magnetic moments as arrows.*

Magnetic Phases II and III. The magnetic ordering vector of Phase II is identified as **U** (0, 2/3, 1/2). According to representational analysis using ISODISTORT[19], there is one magnetic distortion IR m**U**$_1$ and two independent monoclinic structure models (labelled as m**U**$_1$-1 and m**U**$_1$-2), with magnetic space groups (Shubnikov groups) C_cm (8.35) and C_cc (9.40) respectively. The

transformation matrix from 30 K nuclear structure to the distorted magnetic structure is [(-1, 0, 0), (0, 3, 0), (0, 0, -2)]. There are 31 independent modes in m**U**$_1$-1 and 32 in m**U**$_1$-2 for the magnetic ordering models. Using a similar parameter analysis as for Phase I, three key independent parameters of four modes for each model were identified. The R_{wp} factors from the refinement of m**U**$_1$-1 and m**U**$_1$-2 model against the 7.5 K NPD data are very close: 5.48% with all modes refined and 5.59% with four key modes (three parameters) refined, for both models. Thus, it is impossible to distinguish the two models from the available data and both three-parameter four-mode models give reasonable descriptions of the magnetic structure of Phase II. The profiles from Rietveld refinements using the m**U**$_1$-1 and m**U**$_1$-2 models against the 7.5 K NPD data are shown in Fig. 9, both yielding excellent fits to experimental data. These two magnetic structures refined against the 7.5 K NPD data are shown in Fig. 10, with details given in the magnetic CIF files in the SI. The magnetic ordering of Phase II is similar to that of Phase I (including the zero refined moment on the Ni1 site), but the moment arrangement in the [NiO_6]-[PO_4] layers is different.

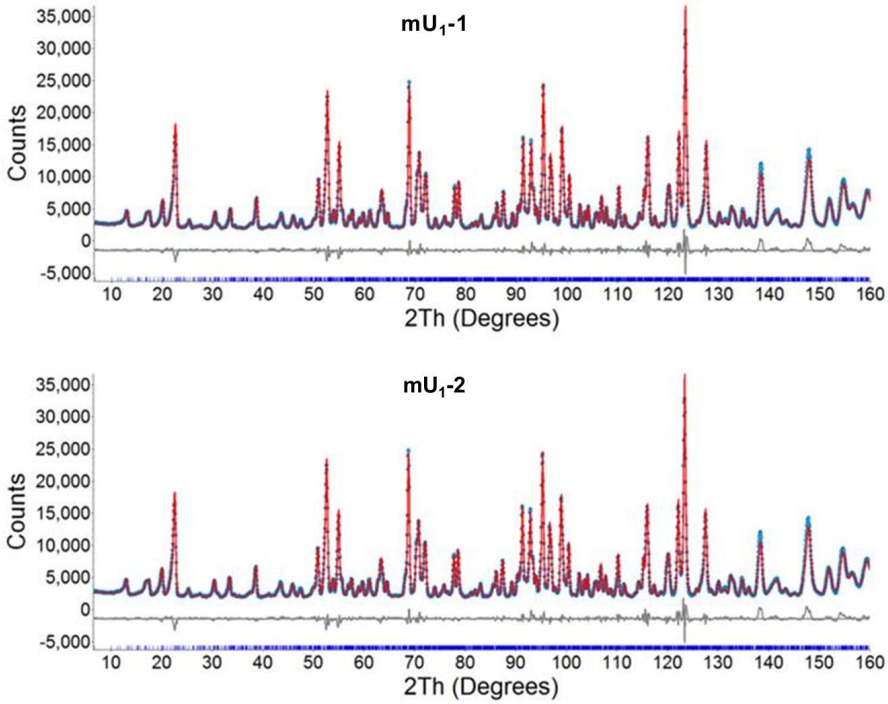

Fig. 9. *Rietveld refinement profiles of $Na_4Ni_7(PO_4)_6$ magnetic Phase II against 7.5 K NPD data using m**U**$_1$-1 and m**U**$_1$-2 models. Dots, observed pattern; solid line, calculated pattern; grey line below, difference curve; vertical tick marks, peak positions.*

The layers in both Phases I and II are built from distinct FM Ni^{2+} stripes with AFM arrangements between them; the difference lies in the amplitude of the moments of those stripes, which are all the same in Phase I but vary in Phase II. In Phase II, the amplitude of the Ni^{2+} magnetic moments is modulated to form a wave-like arrangement which enlarges the period to a 3x supercell along the *b* axis. The Ni^{2+} moments vary from 0-2.1(1) μ_B in m**U**$_1$-1 and from 0-2.5(2) μ_B in m**U**$_1$-2, aligned in the same directions in both phases. This may be caused by competition between thermal perturbation and AFM exchange in the [010] direction, which only exerts itself in the lower temperature regime, highlighting the subtle spin-coupling in this system. The major difference

between models m**U**$_1$-1 and m**U**$_1$-2 is the relative phase shift of this moment wave along the *b* axis (in fact, the two phases are equivalent when considered from the superspace perspective as commensurate modulations). The phase transition from Phase I to Phase II then corresponds to the realignment of the amplitude modulations of the Ni^{2+} moments.

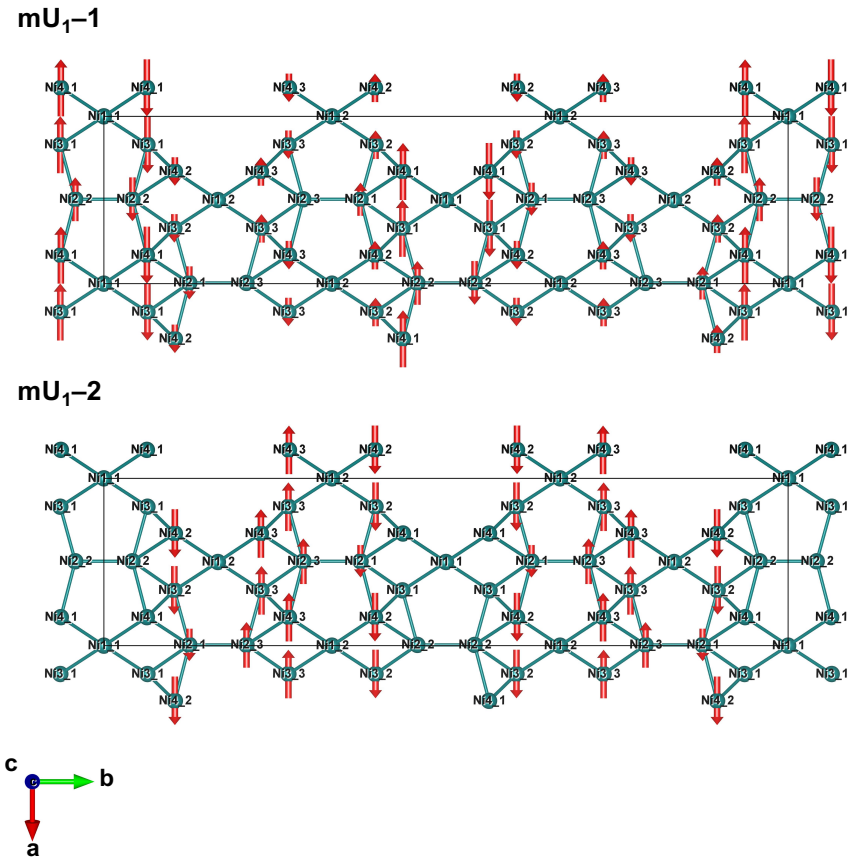

Fig. 10. *Single layers of the Rietveld-refined Phase II magnetic structures of $Na_4Ni_7(PO_4)_6$. Neighboring layers are AFM with respect to those shown. Only Ni sites are shown, with the magnetic moments as arrows.*

Magnetic Phase III can be considered as an incommensurate modulation of the Ni^{2+} moments of Phase II. From Pawley refinements, it requires a *P*-lattice (as opposed to the *C*-lattice in Phase I and Phase II) to describe the Ni^{2+} magnetic moments with at least 24 refineable magnetic wave parameters. Unfortunately, this is not statistically possible, given the limited number of observed magnetic Bragg peaks. Nevertheless, given the very similar magnetic reflection intensity distribution, it is almost certain that Phase III has a similar moment arrangement as Phase II, with an AFM arrangement of FM Ni^{2+} stripes but more complex modulation behavior.

Conclusions

The low-temperature ordering of magnetic moments on Ni^{2+} in $Na_4Ni_7(PO_4)_6$ is remarkably complex. On cooling, it passes through two distinct phases with commensurate k-vectors [0, 1, 1/2] (Phase I, $9.1 < T < 17$ K) and [0, 2/3, 1/2] (Phase II, $4.6 < T < 9.1$ K), before reaching a ground state with an incommensurate k-vector [~0.076, 2/3, 1/2] (Phase III, $T < 4.6$ K). Phases I and II feature

ferromagnetic (FM) stripes arranged in net antiferromagnetic (AFM) 3D structures. The moment amplitudes of all stripes are same in Phase I but vary in Phase II, and the transition between them is accompanied by a release of magnetic entropy according to heat capacity data. Given that the FM stripes are readily explained by nearest neighbor superexchange (SSE) through ~90° Ni–O–Ni pathways, the Phase I → II transition must be due to competing AFM second-nearest and third-nearest neighbor super-superexchange through bridging PO_4 units, the balance of which changes as thermal perturbations are reduced on cooling. An unusual feature of both Phases I and II is the presence of a unique Ni site (labelled Ni1) which lies in a geometrically frustrated position halfway between AFM-coupled FM chains, and consequently has no ordered magnetic moment. Note that while we are confident that the determined long-range spin orderings are correct, further neutron diffraction experiments on single crystals will be required to definitively assign the spin orientations, if and when such crystals become available.

A full solution and refinement of the magnetic structure of Phase III could not be achieved due to its complexity relative to the limited number of observed magnetic Bragg peaks. However, the similarity of the intensity distribution and the absence of a heat capacity peak at the Phase II → III transition temperature points to it being a subtle incommensurate modulation of Phase II, which only emerges at the lowest temperatures from the final balance between competing long-range SSE exchange interactions. Further investigations of Phase III will require significantly higher intensity neutron diffraction data with good resolution at low-Q (*i.e.*, a time-of-flight instrument), ideally accompanied by a detailed *ab initio* (DFT+U) computational study, which lie beyond the scope of the present work.

Supplementary Information

NNPO_30K_NUC.cif, crystallographic information file (CIF) for the nuclear structure of $Na_4Ni_7(PO_4)_6$ at 30 K; NNPO_9p5K_MAG_mM1.cif, CIF for the m$\mathbf{M}_1$ model of magnetic Phase I of $Na_4Ni_7(PO_4)_6$ at 9.5 K; NNPO_9p5K_MAG_mM2.cif, CIF for the m$\mathbf{M}_2$ model of magnetic Phase I of $Na_4Ni_7(PO_4)_6$ at 9.5 K; NNPO_7p5K_MAG_mU1_1.cif, CIF for the m$\mathbf{U}_1$-1 model of magnetic Phase II of $Na_4Ni_7(PO_4)_6$ at 7.5 K; NNPO_7p5K_MAG_mU1_2.cif, CIF for the m$\mathbf{U}_1$-2 model of magnetic Phase II of $Na_4Ni_7(PO_4)_6$ at 7.5 K. SI_Na4Ni7(PO4)6.docx, comparison of direct-current magnetic susceptibility data collected in zero field-cooled and field-cooled modes, and visual representations of the spin configurations labelled as A' A1, A2, A3, A1", A2" in the main text and defined in the deposited CIFs.

Acknowledgements

CDL and MA received support for this work from the Australian Research Council (DP170100269).

References

1. Palomares, V.; Serras, P.; Villaluenga, I.; Hueso, K. B.; Carretero-Gonzalez, J.; Rojo, T., Na-Ion Batteries, Recent Advances and Present Challenges to Become Low Cost Energy Storage Systems. *Energ Environ Sci* **2012**, *5*, 5884-5901.

2. Pan, H. L.; Hu, Y. S.; Chen, L. Q., Room-Temperature Stationary Sodium-Ion Batteries for Large-Scale Electric Energy Storage. *Energ Environ Sci* **2013**, *6*, 2338-2360.
3. Yabuuchi, N.; Kubota, K.; Dahbi, M.; Komaba, S., Research Development on Sodium-Ion Batteries. *Chem Rev* **2014**, *114*, 11636-11682.
4. Kubota, K.; Komaba, S., Review-Practical Issues and Future Perspective for Na-Ion Batteries. *J Electrochem Soc* **2015**, *162*, A2538-A2550.
5. Wang, L. P.; Yu, L. H.; Wang, X.; Srinivasan, M.; Xu, Z. C. J., Recent Developments in Electrode Materials for Sodium-Ion Batteries. *J Mater Chem A* **2015**, *3*, 9353-9378.
6. Fang, C.; Huang, Y. H.; Zhang, W. X.; Han, J. T.; Deng, Z.; Cao, Y. L.; Yang, H. X., Routes to High Energy Cathodes of Sodium-Ion Batteries. *Adv Energy Mater* **2016**, *6*, 1501727.
7. Fang, Y. J.; Zhang, J. X.; Xiao, L. F.; Ai, X. P.; Cao, Y. L.; Yang, H. X., Phosphate Framework Electrode Materials for Sodium Ion Batteries. *Adv Sci* **2017**, *4*, 1600392.
8. Moring, J.; Kostiner, E., The Crystal-Structure of $Na_4Ni_7(PO_4)_6$. *J Solid State Chem* **1986**, *62*, 105-111.
9. Sanz, F.; Parada, C.; Rojo, J. M.; Ruiz-Valero, C., Synthesis, Structural Characterization, Magnetic Properties, and Ionic Conductivity of $Na_4M(II)_3(PO_4)_2(P_2O_7)$ (M (II) = Mn, Co, Ni). *Chem Mater* **2001**, *13*, 1334-1340.
10. Sanz, F.; Parada, C.; Rojo, J. M.; Ruiz-Valero, C., Crystal Structure, Magnetic Properties, and Ionic Conductivity of a New Mixed-Anion Phosphate Na_4Ni_5 $(PO_4)_2(P_2O_7)_2$. *Chem Mater* **1999**, *11*, 2673-2679.
11. Ben Yahia, H.; Shikano, M.; Kobayashi, H.; Avdeev, M.; Liu, S.; Ling, C. D., Structural Relationships among $LiNaMg[PO_4]F$ and $Na_2M[PO_4]F$ (M = Mn, Ni, and Mg), and the Magnetic Structure of $LiNaNi[PO_4]F$. *Dalton T* **2014**, *43*, 2044-2051.
12. Barpanda, P.; Avdeev, M.; Ling, C. D.; Lu, J. C.; Yamada, A., Magnetic Structure and Properties of the $Na_2CoP_2O_7$ Pyrophosphate Cathode for Sodium-Ion Batteries: A Supersuperexchange-Driven Non-Collinear Antiferromagnet. *Inorg Chem* **2013**, *52*, 395-401.
13. Orayech, B.; Ortega-San-Martin, L.; Urcelay-Olabarria, I.; Lezama, L.; Rojo, T.; Arriortua, M. I.; Igartua, J. M., The Effect of Partial Substitution of Ni by Mg on the Structural, Magnetic and Spectroscopic Properties of the Double Perovskite Sr_2NiTeO_6. *Dalton T* **2016**, *45*, 14378-14393.
14. Yogi, A.; Bera, A. K.; Maurya, A.; Kulkarni, R.; Yusuf, S. M.; Hoser, A.; Tsirlin, A. A.; Thamizhavel, A., Stripe Order on the Spin-1 Stacked Honeycomb Lattice in $Ba_2Ni(PO_4)_2$. *Phys Rev B* **2017**, *95*, 024401.
15. Munsie, T. J. S., et al., Neutron Diffraction and Mu Sr Studies of Two Polymorphs of Nickel Niobate $NiNb_2O_6$. *Phys Rev B* **2017**, *96*, 144417.
16. Avdeev, M.; Hester, J. R., Echidna: A Decade of High-Resolution Neutron Powder Diffraction at Opal. *J Appl Crystallogr* **2018**, *51*, 1597-1604.
17. Evans, J. S. O., *Extending the Reach of Powder Diffraction Modelling by User Defined Macros.* Trans Tech Publications Ltd, Zurich; Scardi, P., Dinnebier, R. E., Eds.; **2010**; Vol. *651*, pp 1−9.
18. Coelho, A. A.; Evans, J. S. O.; Evans, I. R.; Kern, A.; Parsons, S., The Topas Symbolic Computation System. *Powder Diffr* **2011**, *26*, S22-S25.
19. Campbell, B. J.; Stokes, H. T.; Tanner, D. E.; Hatch, D. M., Isodisplace: A Web-Based Tool for Exploring Structural Distortions. *J Appl Crystallogr* **2006**, *39*, 607-614.

Table of Contents Graphic